In Situ X-ray Phase Contrast Imaging of Humping Formation During Laser Beam Welding of 1.4404 Stainless Steel

Elie Haddad*[1], Marie-Cathrin. Lach[2,3], Christoph Spurk[3], Marc Hummel[3], André Häusler[1], Alexander Olowinsky[1], Felix Beckmann[4], and Julian Moosmann[4]

[1]*Fraunhofer Institute for Laser Technology ILT, Aachen, Germany*

[2]*FH Aachen - University of Applied Sciences, Aachen, Germany*

[3]*Chair of Laser Technology LLT, RWTH Aachen University, Aachen, Germany*

[4]*Institute of Materials Physics, Helmholtz-Zentrum Hereon, Geesthacht, Germany*

**Corresponding author's e-mail: elie.haddad@ilt.fraunhofer.de*

Continuous development of laser beam sources and process technologies allows higher welding speeds, partly due to the high focus ability and brilliance of fiber laser sources. However, the increasing interest in cost-efficient production of bipolar plates for fuel cells, for example, poses a challenge due to imperfections, which occur during high-speed welding of metals. A particular defect – referred to as humping in the welding sector – manifests itself in the form of periodical accumulation of solidified melt on the weld bead surface. The main objective of this paper is to establish a basic understanding of humping, which could allow a shift of the effect to higher welding speeds for stainless steel 316L. This is done through tests using in-situ X-ray videographic images. Factors of capillary dynamics and capillary behavior that cause humping are analyzed. Furthermore, attempts to shift the humping limit are investigated using an Adjustable Ring Mode (ARM) laser. With the flexible power control of the core to ring beam, the capillary dynamics and the occurrence of humping are closely examined. Finally, new findings with regards to the indicators for the occurrence of humping and an assessment of the use of an ARM laser to avoid humping are deduced.

DOI: 10.2961/ilmn.2025.01.2001

Keywords: laser welding, stainless steel, humping, welding speed, keyhole dynamics, vapor capillary, X-ray imaging

1. Introduction

Humping is a welding defect, characterized by the forming of seemingly periodic occurring droplets along the surface of the weld seam due to pile-up of the melt and has been observed since approximately 50 years across various welding procedures [1]. In the Albright et al. study from 1988 about welding defects, it is suggested, that the formation of the so-called humps has its roots in unfavorable laser power and welding speed conditions, concluding that for humping to occur, both these must be too high [2]. Zhou et al. attribute the humping formation to the combined effect of the strong melt flow at the vapor capillary, caused by the recoil pressure of the laser, and a fast solidification rate [3]. Kawahito et al. identify among other things the volume of melt on the surface, the intensity of the molten pool dynamic and other hydrostatic and hydrodynamic factors as decisive characteristics for this phenomenon [4]. According to Fabbro, the five main regimes in laser welding are defined by the penetration depth depending on the welding speed. These regimes are limited to certain welding speeds and can be defined as follows: "Rosenthal" at welding speeds below 5 m/min (about 83 mm/s), "single-wave" between 6 and 8 m/min (100-133 mm/s), "elongated keyhole" between 9 and 11 m/min (150-183 mm/s), "pre-humping" between 12 and 19 m/min (200-317 mm/s) and "humping" above 20 m/min (333 mm/s). This concludes that the humping effect can be observed starting welding speeds of 333 mm/s [5]. Yuewei et al. describe the requirements for humping in the tilt angle of the vapor capillary, the reduced molten pool width on the sides and in front of the keyhole as well as an unfavorable flow dynamic behind the keyhole at higher welding speeds [6]. Zhang et al. work out four decisive factors of vapor capillary and weld pool dynamics from their investigation of hump formation during laser welding of stainless steel. According to Zhang, the melt flow driven by the recoil at the bottom of the keyhole is one of the main triggers for humping. Furthermore, the surface tension and the advancement speed of the solidification front at the bottom of the melt pool, as well as local solidification in the rear melt pool, are responsible for the size and periodicity of the humps [7].

In laser micro welding of stainless steel, the interaction between the melt flow and the solidification front is complex and involves several interrelated mechanisms. These mechanisms significantly influence the stability of the weld pool and contribute to phenomena such as humping. Primary mechanisms involved are thermal gradients and fluid flow, solidification dynamics, heat transfer effects and material specific factors.

Despite several studies, the humping effect still poses a challenge in welding with higher speeds, particularly in stainless steel, mainly due to a lack of full-scale understanding of and an inability to visualize the effects taking place. The work carried out in this paper allows – through the use of X-ray contrast imaging – new insights into the events taking place in a cross-section of the keyhole during the laser welding process and the formation of the humps. Additionally, the use of a ring-mode fiber laser to influence the keyhole geometry and shift the humping limit towards higher welding speeds is investigated.

2. Theory

2.1 Welding regimes in laser micro welding

In laser micro welding, two regimes are defined based on the temperatures reached and the aspect ratio of the weld seam. In heat conduction welding, the heat conduction is the main influencing factor behind the seam formation. The evaporation temperature of the material is not reached and the aspect ratio – ratio of weld seam width to weld seam depth – remains below 1. In deep penetration welding – also called keyhole welding – the evaporation temperature of the material is surpassed. A vapor capillary, also referred to as keyhole, forms and the factors influencing it define the welding result. The aspect ratio of the weld seam is also significantly increased and could reach 10:1, due to increased energy absorption into the material through multiple reflections on the walls of the vapor channel [8].

2.2 Vapor capillary and molten pool dynamics in the humping formation

The occurrence of the humping phenomenon can be attributed to four main aspects: fluid dynamics in the melt pool, the geometry of the vapor channel and melt pool, the surface tension and material properties such as thermal diffusivity and temperature difference between evaporation and melting point [9]. The geometrical aspects and the flow behavior in the vapor capillary and the surrounding molten pool are used as tools to attempt a more extensive explanation for the occurrence of the humping phenomenon. Based on the literature and examinations available to this topic, the formation of humps can be summarized in three main factors [10]:

- melt accumulations occur at the rear end of the molten pool.
- the formation of humps depends on high flow speeds in the molten pool.
- the high flow speeds in the molten pool can be attributed to the ablation pressure at the keyhole front

A general model, developed by viewing several studies, cites the occurrence of solidification and deflection processes in the lower area of the melt pool near the vapor channel as the main cause. At a low welding speed, the welding process is predominantly influenced by thermal effects resulting in a nearly circular keyhole geometry and a relatively large melt pool [1]. With increasing welding speed and under the direct influence of the vapor on its rear wall, the keyhole is stretched while simultaneously a melt wave emerges behind it [11]. The high aspect ratios, typical for keyhole mode in micro welding encourage solidification starting from the side edges of the weld pool, and thus a progressive shortening of the lower weld pool length [12]. Figure 1 shows schematically the formation of humps with an increasing welding speed. When the part of the melt flowing downwards around the vapor channel meets the shortened lower melt pool, it is accelerated strongly in the direction of the surface (Figure 1a). The melt stream accelerated laterally around the capillary meets the strongly accelerated main melt stream flowing in from below. The converging melt streams are deflected backwards. This altered flow geometry results in the formation of a "melt jet" in the middle of the melt pool with significantly increased flow velocity.

However, this melt jet can only spread over a certain length, restricted by the so-called Rayleigh instability, leading to a local narrowing of this jet. The Plateau-Rayleigh instability assumes that the melt pool is a cylindrical fluid jet, with an infinite radius R, freely suspended in space and only maintained by surface tension [13].

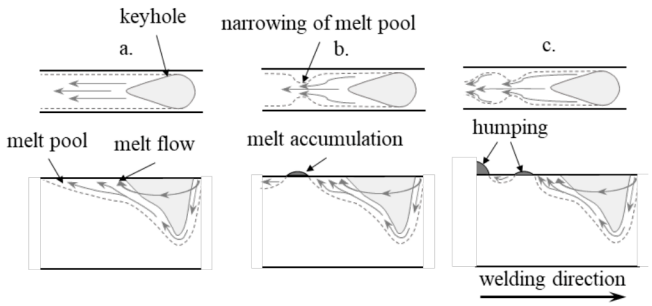

Fig. 1 Humps formation depending on the flow behind and around the keyhole.

Due to the surface tension, the liquid jet disintegrates into a droplet chain (Figure 1b). Equation 1 is used as the instability criterion for the liquid jet to express the critical length $L_{crit.}$, where v represents a certain speed and R the half-width of the weld seam, ϱ the material density and σ the surface tension [13]:

$$L_{\text{crit}} = 3v\sqrt{\frac{\rho}{\sigma}R^3} \qquad (1)$$

This equation shows that the tendency to decay increases with long, slender weld pools and that the conditions for humping are therefore particularly present in micro welding with small focus diameters and high welding speeds.

During high-speed welding, the velocity of the molten metal in the weld pool often significantly exceeds the welding speed. This imbalance leads to incomplete filling of the weld groove. As the molten metal flows along the weld groove, it begins to solidify from the sidewalls. This changes the cross-sectional area available for the remaining molten metal to flow. The narrowing of the flow channel forces the remaining molten metal to deflect upwards. This upward flow contributes to the initial formation of a hump. The conservation of mass in the (assumed) incompressible molten material ensures that regions with smaller cross-sections along the weld are balanced by regions of larger cross-sections, appearing

as humps. Surface tension effects further shape the hump by pulling the molten material towards the forming hump. At the melt pool's end, stagnation of the high-speed melt jet contributes to the hump's growth. The interaction between vapor flow, keyhole dynamics, and the molten material adds momentum to the melt. This momentum, along with factors like cooling rates and thermal expansion, influence the position and size of humps. The periodicity of humping is observed as the distance between successive humps in the weld bead. This distance decreases with an increase in welding speed [11]. A simplified depiction of this is illustrated in Figure 1c. The periodic nature of humps results from a balance between the melt flow's dynamic pressures, cooling rates, and solidification. Periodic underfill regions from between humps due to insufficient material. Surface tension pulls material into the hump while thermal gradients influence solidification rates. These combined effects as well as welding parameters (spot diameter, welding speed) and specific material properties dictate the final size and shape of the hump [1]. In the works of Fabbro in [14] and [15], humping is attributed to the formation of a high-speed liquid strip jet localized at the bottom of the weld groove and is defined by the moving keyhole front surface [14]. This liquid strip jet undergoes the Rayleigh instability. Another important aspect is the inclination of the keyhole front wall, which affects the evaporation zone [15]. At higher welding speeds, the keyhole is inclined and in the "pre-humping" regime, the intensity impinging this surface is much higher than at lower speeds. The vapor plume can be assumed to be very dense and dynamic, that it leads to a rearward acceleration of the melt flow. This flow is assisted by the lateral ejection of melt from the underneath the keyhole front wall [14, 15]. The role of the keyhole front wall is further highlighted in [16]. The molten metal flows downward on the front face of the keyhole, which is crucial for transporting the molten material from the front to the weld pool behind the keyhole. Through measuring the flow speed of surface ripples on the liquid metal, a discrepancy is found. The flow speeds are between two and four times as high as the theoretical average fluid flow rate. The inclination angle of the keyhole front and the behavior of the melt flow are influenced by welding parameters such as welding speed, laser power, and material properties. Adjustments in these parameters affect the melt flow dynamics and subsequently the quality of the weld. [16].

3. Experimental setup

The experimental setup for this work is based on using the high energy beamline P07 (EH4) of Petra III at Deutsches Elektronen Synchrotron DESY in Hamburg, Germany [17]. To observe the welding process, the X-ray radiation is transmitting the metal sample and is detected by a GaaGG:Ce (Cerium doped Gadolinium Aluminium Gallium Garnet) scintillator. Using an i-Speed 727 high-speed camera, the intrinsic glow of the scintillator screen stimulated by the X-rays is recorded. The pictures are taken with 1600 x 900 pixels at a frame rate of 10 kHz and 1 ms exposure time. The data on synchrotron radiation and the camera setup for the experiments can be found in table 1.

Table 1 Characteristics and parameters of the synchrotron and the used setup [18].

Parameter	Unit	Value
Operating mode	[-]	High beta
Photon energy	[keV]	74
Radiated area	[mm²]	2 x 2
Scintillator material	[-]	GaaGG:Ce
Scintillator size	[mm²]	11 x 11
Scintillator thickness	[µm]	1200
Distance scintillator to sample	[mm]	~ 3500
Frame rate	[Hz]	10000
Frame size	[Pixel]	1600 x 900

To generate the desired high-speed images, the sample must be moved along a high-speed axis at the required welding speed through the intersection of the laser and the synchrotron beam. The experimental setup for this investigation is shown in Fig. 2. This setup is developed at the Chair of Laser Technology at RWTH Aachen University and the Fraunhofer Institute for Laser Technology ILT [18].

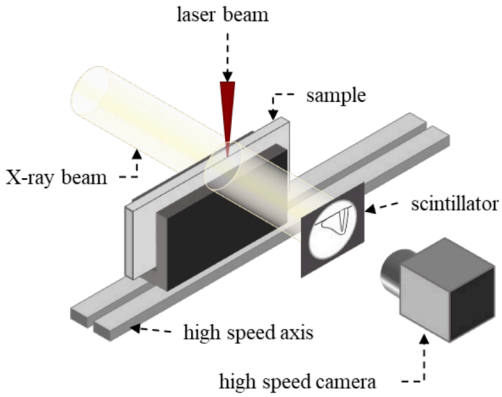

Fig. 2 Experimental setup for the in-situ X-ray phase contrast imaging of the laser welding process.

An Adjustable Ring Mode laser (Highlight FL-4000CSM-ARM) from Coherent, USA is used for the experiments. This laser has a single-mode core beam and a concentric and separately adjustable ring beam. With a wavelength of 1070 nm, the ARM laser can emit at a maximum laser power of 1,5 kW in the core and 2,5 kW in the ring beam. To focus the laser beam at the specimen surface, a f-theta lens with a focal length of 163 mm is used. The welding process is conducted at the focal point of the laser beam. The ring-mode laser beam has an outer beam diameter of 536 µm. The single-mode laser beam is positioned at the center of the ring-mode laser beam and has a beam diameter of 48 µm. The measured Rayleigh length – during the caustic measurement of the core beam – is 1 mm.

For the investigations carried out in the scope of this paper, the material and sample size are kept constant. The work-piece sample has a length of 100 mm and a height of 30 mm. The thickness of the sample must be kept as low as possible for the transmission of X-rays and is 2 mm. The material used is an austenitic stainless steel with the material number 1.4404, also known as AISI 316L or X2CrNiMo17-12-2. This stainless steel is suitable for welding and is corrosion-resistant, making it suitable for the production of metallic bipolar plates, among other things. However, precise process control is required, as the stainless steel has a lower limiting speed for the occurrence of the humping phenomenon due to higher capillary flow velocities. The chemical composition for 1.4404 is listed in Table 2 [19].

Table 2 Chemical composition of stainless steel 1.4404 in wt % [19].

Chemical composition in wt %	
C ≤	0,03
Cr	16 – 18
Ni	10,00 – 14,00
Mo	2,00 – 3,00
Mn ≤	2,0
P ≤	0,045
Si ≤	1,0
S ≤	0,03
Fe	bal.

3.1 Visual analysis of keyhole geometry and changes using synchrotron radiation

The in-situ high-speed recording of the experiments consists of a sequence of grayscale images. To achieve the best possible visualization of the process, a recording frequency of 10000 Hz is used, whereby the high recording frequency makes image post-processing necessary. First, the image quality is improved using a shading algorithm that reduces the background noise caused by the X-ray beam. To enhance process differences during operation, delta images are computed by subtracting denoised images from the initial sample image. Missing material in form of gaseous displacement (pores, keyhole) and density shifts in molten areas get accentuated. A benefit is the removal of static defects of the optical system such as burning on the scintillator, lenses, and banding artifacts of the line scanning camera. However, thermal expansion and material expulsion lead to dark artifacts above the initial sample surface. Using the example of a single in-situ high-speed contrast image shown in Fig. 3, the results of the image post-processing can be seen, the image components can be identified, and the evaluation criteria measured can be defined. The welding direction remains the same during the entire test series. The image shows the longitudinal section of the vapor capillary during welding. The effects of the ring architecture of the laser on the material and on the occurrence of humping are henceforth evaluated using these images. Unfortunately, it is not possible to view the phase transition from liquid to solid, so the melt pool remains invisible. Some experiments with tracer particles or a tracer material are planned to attempt the visualization of the flow.

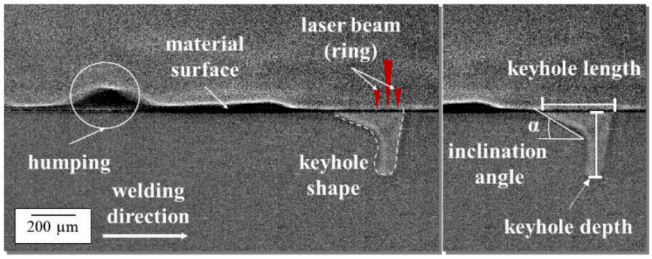

Fig. 3 Shaded X-ray phase contrast image and the used evaluation criteria.

3.2 Experimental parameters

Testing parameters are drawn up on the basis of previously conducted preliminary tests to narrow down the parameter window and can be divided into two main test groups: the first group, where the effect of the ring laser on the melt pool and vapor capillary geometry are to be investigated at a constant welding speed of 1000 mm/s, a core power of 400 W and a ring power that increases by 100 W or 200 W per test. Using the first sample without ring power as a reference, the formation dynamics of humping are studied based on the X-ray videographic images. As the ring power increases, the capillary and melt pool dynamics are increasingly influenced and the changed capillary geometry and thus the possible consequences for the humping formation are evaluated. In the second test group, the welding speed is varied from 1000 mm/s to 1600 mm/s in 200 mm/s increments while maintaining the same core and ring power. Delaying or avoiding humping by using ring power and the changes to the shape of the vapor capillary depending on the welding speed are here particularly investigated.

4. Results and discussion

4.1 Capillary dynamics during humping

The investigation into the occurrence of humping using X-ray videographic images is based on a welding parameter set with a core beam power of 400 W and a welding speed of 1000 mm/s. Humping is subject to a periodicity, which can clearly be observed at the selected speed of 1000 mm/s. Figure 4 shows a 3D surface image with a chromatic height gradient, which illustrates the regularity of the phenomenon in terms of distance and height.

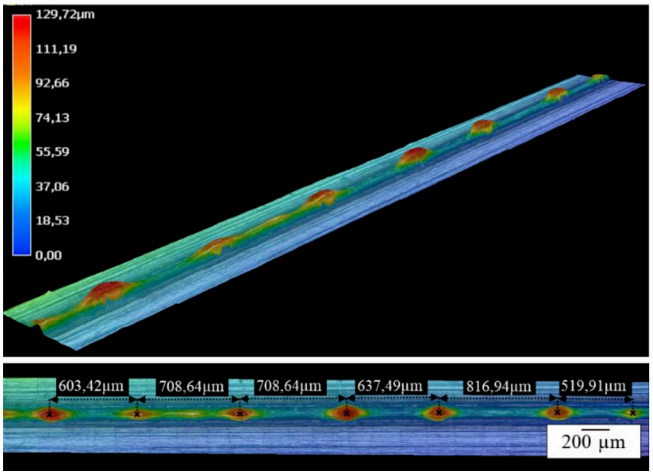

Fig. 4 Surface topography and overview image of a humping ridden welded sample with no ring power, P_{core} = 400 W, v = 1000 mm/s.

The distances between the individual humps are also shown. The average distance between the peak of two humps in this sample is 0,466 to 0,505 mm, further confirming the regularity of the humping phenomenon. The average height of the humps is between 0,060 and 0,1 mm. Figure 5 shows that a welding depth of approx. 0,270 mm is achieved with a core power of 400 W, the gray line in the image has been included to highlight the welding depth.

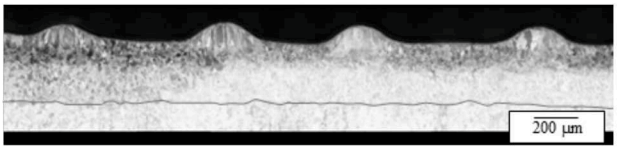

Fig. 5 Longitudinal section of a sample with humping using no ring power, P_{core} = 400 W, v = 1000 mm/s.

4.2 Image sequence analysis of critical humping features

In the following, an analysis of the keyhole dynamics and critical features that promote or cause the development of humping are worked out using an image sequence of the X-ray images. Figure 6 shows an overview of the image sequence for the development of humping, consisting of six images (A-F). A closer look at this overview reveals changes in the capillary geometry over the course of the image sequence. The keyhole length and its rear inclination angle are visibly influenced by the humping dynamics. When comparing Figure 6B and E, a change in the keyhole length becomes visible.

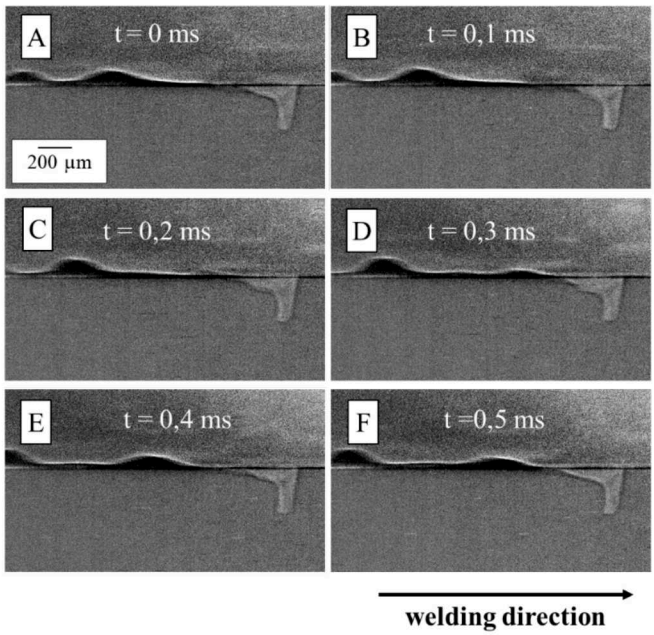

Fig. 6 Image sequence of humping formation, P_{core} = 400 W, v = 1000 mm/s, Δt = 0,1 ms.

For better comparability, each two images of the image sequence (A-B, C-D, E-F) are shown larger next to each other. In these images, the capillary boundary is marked with lines and arrows so that the sequence of changes in the geometry can be traced based on the changing pattern.

The keyhole in Figure 7A has a length of 0,345 mm and a rear angle of inclination of 20°. As a result of the high flow velocities that stainless steel assumes, the downward-flowing and accelerated portion of the melt around the capillary result in unsteady capillary changes. The flat geometry of the keyhole reduces this turbulent flow, as the melt is directed backwards, almost parallel to the surface.

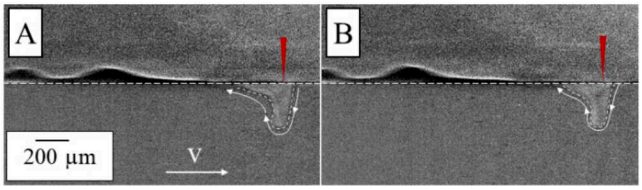

Fig. 7 Images A and B showing the humping development analysis with A: t = 0 ms and B: t = 0,1 ms.

Figure 7B shows a change in the capillary geometry that appears to be decisive for the occurrence of humping. The capillary length is shortened to 0,283 mm and the rear part of the capillary assumes a steeper angle of 29°. The sudden and significant shortening of the capillary length and the steeper angle of inclination result in a possible disturbance of the flow compared to Figure 7A. The transport of the melt to the surface is steeper and faster, reaching the critical formation point for humping. A possible explanation for the sudden shortening of the vapor capillary by 0,060 mm is the Plateau-Rayleigh instability, which describes the disintegration of a liquid jet into a droplet chain.

The smaller beam diameter (50 µm) causes a smaller weld pool and consequently a smaller weld seam width, causing R in the equation (1) to be reduced. This leads to a reduction of the critical humping length and the humping threshold to be pushed to lower welding speed values. A narrowing of the melt channel behind the capillary leads to a build-up of rapidly approaching melt, which results in a shortening of the capillary and a steeper angle of inclination. The result of this change in geometry is shown in Figure 8C, where the curvature of the capillary geometry continues upwards and reaches a maximum angle of inclination at 31°, and the length of the capillary increases to 0,309 mm. Furthermore, the change of the geometry can be described as further bulging at the rear, as shown by the arrows. It can be assumed that the melt is further accelerated upwards by the steeper angle and the bulging, as it is not possible for it to flow backwards due to the narrowing of the channel, caused by the increase of the welding speed, as described in 2.2, and effects from the surface tension. This leads to an accumulation of solidifying melt on the seam surface, which can be seen shortly behind the capillary. Figure 8D shows, with a further increase in capillary length of 0,332 mm and a slight decrease in the keyhole rear inclination angle to 29°, no further changes take place, except for a stronger bulging, which is presumably followed by intensified melt accumulation. This can be seen in the increasing formation of a humping droplet shortly behind the elongated keyhole.

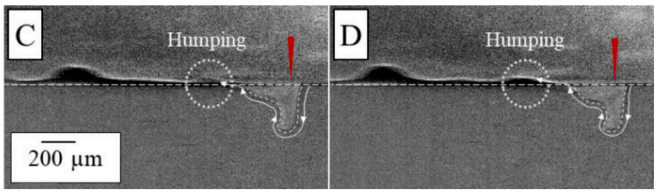

Fig. 8 Images C and D showing the humping development analysis with C: t = 0,2 ms and D: t = 0,3 ms.

A decrease in the effect described from Figure 8C can be observed from Figure 9E onwards. The capillary length increases to 0,348 mm and the bulging is decreased with an angle of inclination of 27°. As can be seen in the image, the hump continues to grow as the melt flows at a higher speed than the welding speed. One possible reason for the regression of the geometry would be the increasing distance to the narrowed melt channel, so that the melt flowing around the keyhole accumulates less.

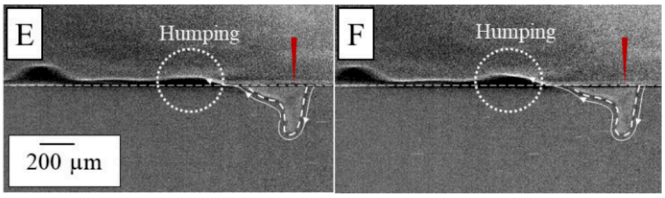

Fig. 9 Images E and F showing the humping development analysis with E: t = 0,4 ms and F: t = 0,5 ms.

Figure 9F concludes the image sequence and shows the capillary geometry after completion of the movement sequence resulting in humping. Droplet growth is not yet complete with this image, but the formation mechanism in the keyhole is complete – for one period – and occurs again within the next few images, just as it does in the last six images. With a length of 0,387 mm, the geometry of the keyhole is longer than that of Figure 6A. The angle of inclination is flattened to 19° and thus also lower than it is in Figure 6A.

4.3 Humping in correlation with the vapor capillary geometry

If the data for the capillary length, the capillary depth, and the rear inclination angle from the image sequence in Figure 6 are graphed, the correlation between these three characteristics and the occurrence of humping becomes clearly visible. This is illustrated in the graph in Figure 10.

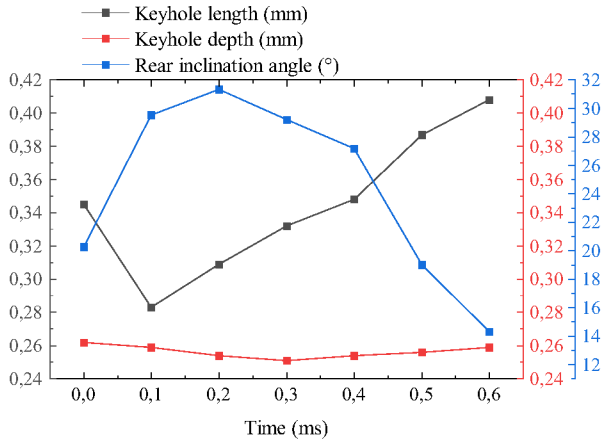

Fig. 10 Comparison of the keyhole length, depth, and the rear inclination angle from the image sequence without ring power.

This graph shows the changes occurring on the keyhole level during the time period of a single hump. The depth of the keyhole doesn't show major fluctuation between the singular images, however along the entire sequence, it can be seen, that a reduction of 0,011 mm occurs from 0,262 mm in Figure 6A to 0,251 mm in Figure 6D followed by an increase of 0,08 mm to 0,259 mm. The keyhole length shows a different behavior, reaching its lowest value at 0,283 mm (t = 0,1 ms) in Figure 6B and then only an increasing trend up to 387 µm in the last image of the sequence. In a further image, which is not shown here, it even increases up to 0,408 mm (at 0,6 ms), so a total difference of +0,125 mm. Contrary to the keyhole length, the rear inclination angle shows a fluctuation, initially increasing up to its maximum value of 31,3° at t = 0,2 ms, and then decreasing to 14,3° at t = 0,6 ms. This leads to the conclusion, that during humping, the sudden shortening of the keyhole length causes an increase in the keyhole rear inclination angle.

Based on the data from Figure 10, it can be said, that avoiding the sudden shortening of the keyhole length and consequently keeping the rear inclination angle more or less constant, should stabilize the dynamics of the capillary, which lead to the occurrence of humping. The observations from the shown image sequence and the data projected onto the graph in Figure 10 are also observed at different time stamps and samples with humping. However, due to factors influencing the weld seam and complex interaction between laser beam and material, which cannot be visualized in these

videos, it cannot be concluded, if the sudden shortening is the cause or a consequence. Other investigations to prove the validity of the theory of the Rayleigh instability in this particular case are also necessary.

4.4 Influencing the keyhole dynamics with an ARM laser

In the following, the effect of the Adjustable Ring Mode architecture at a constant welding speed and continuously increasing ring power is examined. The evaluation criteria are the keyhole depth, length, and rear inclination angle. Figure 11 shows an image sequence similar to the one shown in Figure 6 but with an applied increasing laser power in the ring, while keeping the other parameters such as power in the core and welding speed constant at consequently 400 W and 1000 mm/s.

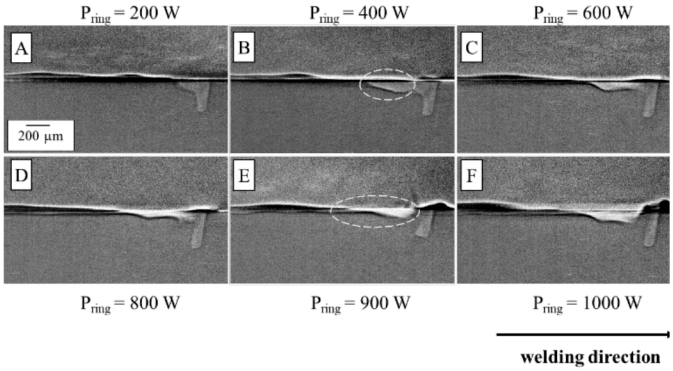

Fig. 11 Image sequence showing the changes in the keyhole shape with increasing ring power at a constant welding speed, P_{core} = 400 W, v = 1000 mm/s.

Starting with 200 W in Figure 11A, the power in the ring is increased by 200 W increments to reach 800 W in figure 11D and for a more detailed observation in 100 W increments after that to 1000 W in Figure 11F. Significant changes with regards to the shape and development of the keyhole and consequently the molten pool are observed. In contrast to the trials with no ring power, the depth shows an increasing trend proportional to the increasing ring power. Besides the depth, the keyhole is reshaped with sufficient power (starting 400 W) and now consists of an overlap of both capillaries caused by the core and the ring beams, significantly elongating the formed combined keyhole. Finally, when the ring power becomes too high, a detachment of the capillaries occurs, and the molten pool appears to become less stable with some spatters and melt accumulation occurring near the front of the keyhole caused by the core beam.

The data for the evaluation criteria is depicted in figure 12 analogously to the evaluation of the earlier image sequence. The measurements are an average of 12 random samples at different time stamps in the image sequence.

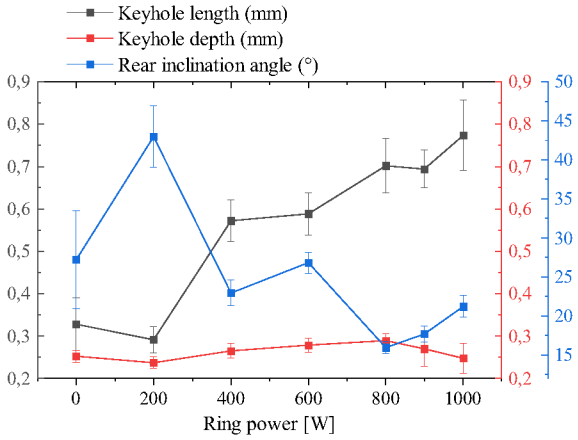

Fig. 12 Comparison of the keyhole length, depth, and the rear inclination angle from the image sequence with increasing ring power at a constant welding speed, carried out over 12 different samples with the error bars representing the standard deviation.

The keyhole depth increases, with a downward break at 200 W, up to a ring power of 800 W. This is followed by a reversal of the curve, as the depth decreases from then on as the ring power further increases. At a ring power of 900 W, the depth is 270 µm, at 1000 W in the ring it is only 0,247 mm, which is even less than the keyhole depth without ring power. One explanation for the shape of this curve is that at > 800 W, the ring power is too high. The additional high power increases the energy absorbed by the workpiece, resulting in a widening of the keyhole opening and thus a decreasing keyhole depth. A further indication, that the selected ring power is too high, is the sharp increase in the standard deviation, which illustrates the instability occurring, when the power is further increased.

A steady increase in keyhole length can be observed with increasing ring power. In comparison to only using power in the core, where the average length is 0,328 mm, it reaches a maximum of 0,773 mm at 1000 W ring power. This difference of 0,445 mm clearly illustrates the influence of the ring power on the overall geometry. An exception is observed at a ring power of 200 W, where a decrease in keyhole length of 0,037 mm to 0,291 mm (in reference to no ring) is observed.

The behavior of the keyhole rear inclination angle can also be seen in figure 12. Here, the standard deviation is of particular interest. The angle of inclination with only core power applied is 27° and shows a standard deviation of 6°, showing large fluctuations due to the occurrence of humping, which makes a comparison with the subsequent samples difficult. However, the high standard deviation occur-ring here suggests that there is a dependency between the occurrence of humping and the fluctuations of the rear inclination angle. Here, what is additionally striking, is the large jump in the angle of inclination to 43° at a ring power of 200 W, which flattens out again to 21° at 400 W. The lowest value of the inclination angle is measured at a ring power of 800 W (16°). It then increases again to 21° at 1000 W. The flatter angle of inclination achieved by the ring power can help avoid the humping effect due to more stable melt pool dynamics. Also interesting for the process is the decrease in the standard

deviation down to a deviation of 0.8° at 800 W, which indicates a keyhole geometry that becomes more stable with increasing ring power. At > 800 W there is a further increase in both the inclination angle and the standard deviation, which, as before, can be explained by a ring power that is too high for the process, as the keyhole(s) instability increases with increasing ring power.

4.5 Shifting the humping threshold

Figure 13 shows the top view of the weld seams at 0 W ring power and at 200 W ring power, both welded with a speed of 1000 mm/s. In comparison, it can be said that humping no longer occurs even with a power of 200 W in the ring. An increase in the weld seam width is caused by the higher material absorption due the preheating caused by the power applied in the front part of the ring, which is leading the core beam. The decrease of the capillary depth observed in figure 12A is a further confirmation of this explanation. However, the power in the ring is not sufficient to cause the material directly irradiated by the ring beam to melt.

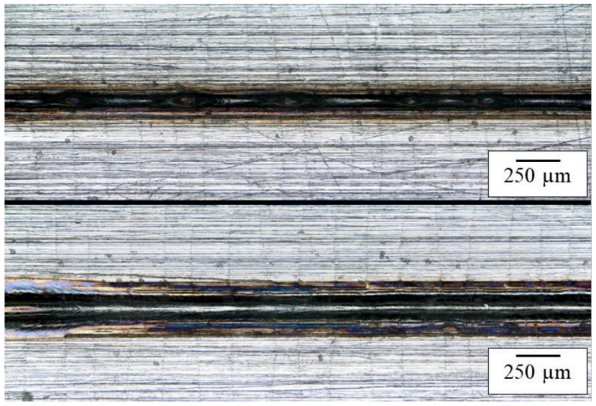

Fig. 13 Overview images showing the effect of minimal ring power on the welding result, P_{core} = 400 W, v = 1000 mm/s, top image: P_{ring} = 0 W, bottom image: P_{ring} = 200 W.

Looking at the data in figure 12, it can be concluded, that it is not the size of the keyhole rear inclination angle itself, but the fluctuations during the welding process that encourage humping to occur, highlighted here through the standard deviations. Furthermore, a possible explanation for the suppressing of the humping effect is the pre-heating and post-heating due the ring beam, which influences the surface tension, which is also a factor in humping formation confirming the findings in [9, 13].

The effect of the ring on the capillary geometry investigated in the first series of tests also influences the humping tendency of the material at higher power. Figure 14 shows two weld seams, welded with 400 W (top image) and 800 W (bottom image) in the ring. With a ring power of 800 W, a more even and slender seam without fluctuations in the weld seam width can be achieved, free of humping. From the previously analyzed data at this ring power, it can be observed, that the keyhole depth reaches its maximum at 0,289 mm. A ring power of 800 W with maximum penetration depth simultaneously ensures an improved flow due to the low keyhole rear inclination angle, which effectively suppresses humping at a welding speed of 1000 mm/s and produces a uniform seam.

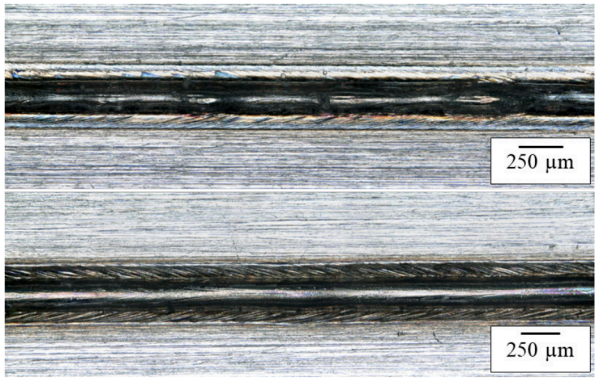

Fig. 14 Overview images showing the effect of increased ring power on the welding result, P_{core} = 400 W, v = 1000 mm/s, top image: P_{ring} = 0 W, bottom image: P_{ring} = 800 W.

5. Conclusion

In the scope of this paper, X-ray videographic high-speed images are used to closely analyze the motion dynamics of the vapor capillary, when humping occurs at 1000 mm/s and then the effect of using a ring mode laser. A repetitive motion structure is identified, which occurs right before the formation of a seam elevation and can be attributed to a combination of a steeper keyhole rear inclination angle, a resulting shortened keyhole length, and subsequent flattening of the inclination angle. Using a ring-mode laser influences the geometry of the vapor capillary: with enough power in the ring beam, the observed keyhole is significantly lengthened in comparison to using only the core beam. The stability of the keyhole and thus the formation of humping depends on the amount of applied power in the ring. With minimal ring power, no keyhole caused by the ring is observed. At 800 W in the ring beam, the keyhole shows a very stable behavior. At powers > 800 W the keyholes from the ring and the core beam separate and the welding process is negatively affected since an increase in spatters and weld surface oxidation are observed. A shift in the humping threshold to higher welding speeds > 1000 mm/s is achieved. Here two different scenarios are observed: using the ring to avoid humping by influencing the surface tension due to pre- and post-heating effects (200 W) and using the ring to enlarge the melt pool around the core vapor capillary (800 W), leading to a larger melt pool and thus allowing the melt a larger cross-section to flow through and reducing the flowing speed, particularly around the vapor capillary. Due to the X-ray analysis, it can be concluded, that controlling fluctuations in the keyhole rear inclination angle and keyhole length can help avoid humping.

Acknowledgments

This work was funded by the German federal ministry for digital and transport in the H2GO project under the funding reference number 03B11027A. The presented investigations were carried out within the cooperation “Laser Meets Synchrotron” (www.laser-meets-synchrotron.de). The

experimental setup and its operation were funded by the Deutsche Forschungsgemeinschaft e.V. (DFG, German Research Foundation) within the framework of the Collaborative Research Centre SFB1120-236616214 "Bauteilpräzision durch Beherrschung von Schmelze und Erstarrung in Produktionsprozessen". The experiments were carried out in cooperation with Helmholtz-Zentrum Hereon in Hamburg at Beamline P07 of DESY PETRA III as part of proposal BAG-20211050 and we would like to thank F. Beckmann, J. Moosmann and all people involved for their support.

Data Availability Statement

The data that supports the findings in this study are available upon reasonable request. Selected data are available after authorization in Coscine with the persistent identifier (PID) http://hdl.handle.net/21.11102/6344f208-a96d-4e06-a6db-6afff084c115 (accessed on July 27, 2024). For further information, please contact the corresponding author.

References

[1] A. Otto, A. Patschger, and M. Seiler: Phys. Procedia, 83, (2016) 1415.
[2] C. E. Albright, and S. Chiang: J. Laser Appl., 1, (1988) 18.
[3] J. Zhou, H. L. Tsai, and P.C. Wang: A.S.M.E., 376 HTD (2), (2005) 945.
[4] Y. Kawahito, M. Mizutani, and S. Katayama: J. Appl. Phys., 40, (2007) 5854.
[5] R. Fabbro: J. Phys. D: Appl. Phys., 43 (44), (2010) 445501.
[6] A. Yuewei, J. Ping, W. Chunming, M. Gaoyang, G. Shaoning, L. Wei, and H. Chu: Opt. Lasers Eng., 107, (2018) 102.
[7] M. Zhang, T. Liu, R. Hu, Z. Mu, S. Chen, and G. Chen: Int. J. Adv. Manuf. Technol., 106, (2020) 5353.
[8] R. Poprawe: "Tailored Light 2" RWTH edition, (Springer, Berlin Heidelberg, 2011) p. 265-275.
[9] A. Patschger, M. Seiler, and J. Bliedtner: J. Laser Appl., 30, (2018) 032409.
[10] P. Berger, and H. Hügel: Phys. Procedia, 41, (2013) 216.
[11] P. Berger, H. Hügel, A. Hess, R. Weber, and T. Graf: Phys. Procedia, 12, (2011) 232.
[12] H. Hügel, and T. Graf: "Materialbearbeitung mit Laser: Grundlagen und Verfahren" 4. Auflage, (Springer Vieweg, Wiesbaden Heidelberg, 2022) p. 369-371.
[13] M. Seiler, A. Patschger, and J. Bliedtner: J. Laser Appl., 28 (2), (2016) 022417.
[14] R. Fabbro, and S. Silmani: Proc. Fourth International WLT-Conference on Lasers Manufacturing 2007, (2007) #259-264.
[15] R. Fabbro, S. Slimani, F. Coste, and F. Briand: Proc. LIM 2007, (2007) #277-282.
[16] I. Eriksson, J. Powell, and A.F.H. Kaplan: Opt. Lasers Eng., 51, (2013) 735.
[17] N. Schell, A. King, F. Beckmann, T. Fischer, M. Müller, and A. Schreyer: Mech. Stress Eval. Neutrons Synchrotron Radiat., VI, (2013) 57.
[18] M.D. Hummel, U. Halm, C. Hagenlocher, J. Lind, S. Hollatz, A. Häusler, et. al.: Proc. LIM 2021, (2021) #1-11.
[19] DIN EN 10088-1:2014-04 Stainless Steels Part 1: List of stainless steels Berlin German Institute for Standardization DIN (2024).

(Received: June 27, 2024, Accepted: December 22, 2024)